STAIG: Spatial Transcriptomics Analysis via Image-Aided Graph Contrastive Learning for Domain Exploration and Alignment-Free Integration

Yitao Yang[1], Yang Cui[1], Sung-Joon Park[2], Xin Zeng[1], Yubo Zhang[1], Martin Loza[2], Kenta Nakai[1,2*]

[1]Department of Computational Biology and Medical Science, the University of Tokyo

[2]Human Genome Center, the Institute of Medical Science, the University of Tokyo

[*] Kenta Nakai (knakai@ims.u-tokyo.ac.jp)

Abstract

Spatial transcriptomics is an essential application for investigating cellular structures and interactions, requiring multi-modal information to precisely study the spatial domains. Here, we propose STAIG, a novel deep-leaning model that integrates gene expression, spatial coordinates, and histological images using graph contrastive learning coupled with a high-performance feature extraction. STAIG can integrate tissue slices without pre-alignment along with removing batch effects. Moreover, it is designed to accept data acquired from various platforms with or without histological images. By performing extensive benchmarks, we demonstrate the capability of STAIG in recognizing spatial regions with high precision and uncovering new insights into tumor microenvironments, which suggests promising potential in deciphering spatial biological intricates.

Introduction

Biological tissues, as intricate networks of varied cell types, perform essential life functions through unique spatial configurations. Recent spatial transcriptomics (ST) techniques, such as 10x Visium[1], Slide-seq[2], Stereo-seq[3] and STARmap[4], have greatly enhanced our ability to map genetic data within these configurations, offering deeper insights into the genetic organization of tissues in health and disease and advancing our grasp of molecular and physiological intricacies.

The ST strongly relies on identifying spatial domains with uniform gene expression and histology. There are two main identification approaches: non-spatial and spatial clustering approaches[5]. Non-spatial clustering methods, such as K-means[6], Louvain[7], and Seurat[8], derive clustering results solely based on gene expression, often resulting in disjointed clusters that poorly reflect the actual spatial patterns of tissues.

Emerging spatial clustering methods like BayesSpace[9] employ Bayesian models to integrate spatial correlations, while SEDR[10] maps gene data using a deep autoencoder combined with spatial information through a variational graph autoencoder. STAGATE[11] utilizes an attention mechanism in a graph autoencoder for adaptive learning of spatial and gene expression data. GraphST[12] leverages graph neural networks with contrastive learning for spot representation. However, these methods do not utilize histological images, such as Hematoxylin and Eosin (HE) stained images, which often results in unclear cluster boundaries and expert annotation misalignment.

Considering these limitations, new methods have been developed to integrate imaging data. stLearn[13] offers a clustering framework using image-derived histological features for gene expression normalization. SpaGCN[14] merges gene expression with spatial and histological pixel data in a weighted graph for graph convolutional network (GCN) analysis. DeepST[15] extracts image features using a neural network to enhance gene matrices. ConST[16] utilizes the MAE[17] visual model to extract histological features, merging them with gene data for domain identification via graph contrastive learning. However, the limited availability of histological images constrains the pretraining of deep models, diminishing their broad applicability and the quality of feature extraction. Furthermore, the extracted features primarily focused on color are often distorted by inconsistent staining, thus limiting their analytical value.

In addition, recent graph-based approaches for ST data are flawed where artificially structured graphs can lead to incorrect neighbor connections. This inaccuracy can disrupt GCNs, compromising result precision. Furthermore, the methods integrating multiple tissue slices, so-called batch integration, require manual alignment of slice coordinates and often overlook the subtle disparities between tissue slices, which still presents challenges to effective integration.

In this study, we propose STAIG (Spatial Transcriptomics Analysis via Image-Aided Graph Contrastive Learning), a deep leaning framework based on the alignment-free integration of gene expression, spatial data, and histological images, to ensure refined spatial domain analyses. STAIG extracts features from HE-stained images using a self-supervised model and builds a spatial graph with the features. The graph is further processed by contrastive learning via a graph neural network (GNN), which generates informative embeddings. We evaluated the performance of STAIG with diverse datasets and found its promising capability in spatial domain identification. We demonstrate that STAIG reveals spatial and genetic details of tumor microenvironments, which advances our understanding of complex biological systems.

Results

Overview of STAIG

To reduce noise and uneven staining, STAIG first segments histological images into patches that align with the spatial locations of data spots, subsequently refining these images with a band-pass filter. Image embeddings are extracted using the Bootstrap Your Own Latent (BYOL)[18] self-supervised model, and an adjacency matrix is simultaneously constructed based on spatial distances between spots (Fig. 1a). To integrate data from different tissue slices, the image embeddings for multiple tissue slices are stacked vertically (Fig. 1b), and the adjacency matrices are merged using a diagonal placement method (Fig. 1c).

Next, from the integrated adjacency matrix, an original graph is built where nodes represent gene expression and edges reflect the adjacency (Fig. 1c). To generate two independent augmented views from this graph, STAIG employs a parallel and independent augmentation process (Fig. 1d). For each augmented view, the process involves randomly removing edges from the original graph, guided by an image-driven probability (or a fixed probability in the absence of images). This is followed by the random masking of gene features, entailing the zeroing of a subset of gene values. Importantly, the probability of edge removal is estimated based on the Euclidean distance of nodes in the image feature space, thus introducing image-informed augmentation into the graph.

The augmented views are processed through a shared GNN guided by a neighbor contrastive objective. This approach aims to closely align nodes and their adjacent neighbors in the two graph views, while distancing non-neighboring nodes (Fig. 1e). Additionally, when images are available, the Debiased Strategy (DS)[19] leverages image embeddings as prior knowledge to ensure nodes that are closer based on image features remain proximate (details in the Method section). Finally, the trained GNN produces embeddings for identifying spatial regions and minimizing batch effects across consecutive tissue slices (Fig. 1f).

Performance in the identification of brain regions

To assess the performance of STAIG in the identification of tissue regions, we prepared the 10x Visium human and mouse brain ST datasets; 12 human dorsolateral prefrontal cortex (DLPFC)[20] slices that were manually annotated into cortical layers L1-L6 and white matter (WM), and the mouse anterior and posterior brain sections. We benchmarked STAIG with the existing methods, such as Seurat, GraphST, DeepST, STAGATE, SpaGCN, SEDR, ConST, and stLearn. To quantify the performance, the Adjusted Rand Index (ARI)[21] for manually annotated datasets and the Silhouette Coefficient (SC)[22] for others were employed (refer to 'Baseline methods and evaluation metrics' in the Supplementary Notes).

Overall, for the human brain datasets, STAIG achieved the highest median ARI of 0.69 across all the slices (Fig. 2a, Supplementary Fig. S1 and S2), particularly, the ARI reached 0.84 in slice #151672 (Fig. 2b). Regarding slice #151673 used in previous studies[23–25], STAIG achieved the highest ARI of 0.68, not only distinctly separating tissue layers L1-L6 and WM in Uniform Manifold Approximation and Projection (UMAP) visualizations, but also closely matching manual labels and accurately recognizing layer proportions (Fig. 2c). In contrast, the results demonstrate that the existing methods provide relatively lower ARIs with misclassified spots and inaccuracies in layer proportions (Fig. 2d-e): stLearn yielded missing a layer and misclassifying spots; GraphST achieved an ARI of 0.64 but had discrepancies in the positioning of layers 4 and 5;

Other methods recorded ARIs between 0.46 and 0.54 due to inaccuracies in layer proportions.

For the mouse posterior tissue dataset (Fig. 2f and Supplementary Fig. S3), STAIG successfully identified the cerebellar cortex and hippocampal region, further distinguishing cornu ammonis and dentate gyrus sections, which is consistent with the Allen Mouse Brain Atlas annotations[26]. In the absence of manual labels, although the overall accuracy was decreased, STAIG achieved the highest SC of 0.31. For the mouse anterior tissue dataset (Fig. 2g and Supplementary Fig. S4), STAIG accurately demarcated areas including the olfactory bulb and dorsal pallium, yielding the highest ARI of 0.44 when we used manual labels from Long et al.[12] as a reference.

Effectiveness of image feature extraction

To investigate the impact of the usage of image features, we applied the k-nearest neighbors algorithm (KNN)[27] algorithm to the image features from STAIG and those from comparison algorithms, i.e., stLearn, DeepST, and ConST. For instance, in the analysis of slice #151507 (Fig. 3a), we found that the image feature from stLearn was heavily influenced by stain intensity and led to mismatches with actual layer annotations. Despite utilizing deep learning models, DeepST and ConST failed to capture the intricate texture characteristic of brain tissues.

Remarkably, STAIG exhibited a high degree of conformity with the texture distribution in manually annotated layers, with only minor deviations attributable to staining variations (Fig. 3a). This precision was particularly evident in the clear demarcation between the WM and Layer 6, as well as the accurate distribution of Layer 3 on either side of Layer 1. Furthermore, the performance of image features from STAIG on slice #151673 was equally impressive (Fig. 3b). Interestingly, the comparative methods for this slice generally succeeded in differentiating only between the WM and non-WM layers, whilst the clustering of STAIG within the non-WM layers aligned closely with manual annotations, especially for Layer 4.

We further investigated the effectiveness of image features with a human breast cancer HE-stained image (Fig. 3c): a pathologist manually annotated regions solely based on the visual interpretation[10]. The results indicate that the image features from stLearn mixed tumor and normal regions and that those from ConST displayed a significant deviation from manual annotations. DeepST failed to capture the image features. Conversely, the STAIG clustering precisely identified the tumor regions and maintained the spatial region coherence in clustering results, suggesting the advanced image feature extraction in STAIG.

Identifying spatial domains without histological image data

As the ST experiments lacking image information is not unusual, we assessed the predictive performances with the datasets where only gene expression and spatial information are available. We initially prepared the mouse coronal olfactory bulb dataset of Stereo-seq[3] annotated through DAPI-stained images[10] (Fig. 4a); the olfactory nerve layer (ONL), glomerular layer (GL), external plexiform layer (EPL), mitral cell layer (MCL), internal plexiform layer (IPL), granule cell layer (GCL), and rostral migratory stream (RMS).

All the algorithms provided the overall trends of spatial stratification for the dataset, while disparities with the annotations were observed (Fig. 4a, Supplementary Fig. S5). For example, Seurat and stLearn failed to distinguish between layers, and STAGATE and GraphST mixed IPL and GCL. DeepST rendered distinct stratifications but failed to discern the GL and IPL layers. Remarkably, STAIG successfully delineated all the layers, even relatively thinner layers, such as MCL and IPL. As shown in Fig. 4b, the expression of layer-specific marker genes[28–33] supported the high-resolution predictions of STAIG that outperformed the existing algorithms (Fig. 4c).

Next, we tested the algorithms using the mouse olfactory bulb tissue dataset of Slide-seqV2[34] (Fig. 4d and supplementary Fig. S6a). The algorithms, except STAIG, GraphST, and STAGATE, struggled to discern the stratification for RMS, accessory olfactory bulb (AOB), and the granular layer of the accessory olfactory bulb (AOBgr). On the other hand, STAIG displayed a higher performance in inter-layer clustering (Fig. 4e), and the results of STAIG were well matched with the expression of layer-specific marker genes[35,36] (supplementary Fig. S6b).

Using a mouse hippocampus dataset[34] from Slide-seqV2 (Fig. 4f and supplementary Fig. S7), we further assessed the methods (Fig. 4f and supplementary Fig. S7). Notably, several methods like Seurat, stLearn, SpaGCN, and SEDR displayed unclear clustering results lacking spatial cohesion. However, STAIG, GraphST, STAGATE, and DeepST delineated spatially consistent clusters for the major anatomical regions, particularly Ammon's horn (CA) was accurately categorized into CA1 and CA3 sections. Again, STAIG recorded the highest SC of 0.40, which was validated by the expression of marker genes[37–39].

Lastly, using the mouse visual cortex dataset of STARmap dataset[4] with inherent annotations, we found that STAIG outperformed all, achieving the highest ARI of 0.67 that markedly surpassed the next best method, STAGATE (Fig. 4g and Supplementary Fig. S8). Moreover, the UMAP plots highlighted the unique ability of STAIG to completely separate all the neocortical layer clusters.

Rebuilding consecutive slices without prior spatial alignment

To test the performance in the vertical slice integration, we used the 12 sections of DLPFC acquired from three individuals. Overall, the existing methods exhibited less effectiveness, particularly, for slices #151508 and #151509 spaced 300μm apart (Supplementary Fig. S9 and S10): DeepST failed to separate the clusters from layers 3-5, and GraphST insufficiently separated layers in the UMAP representation. On the other hand, STAIG successfully integrated these DLPFC slices across various heights (Fig. 5a-b). It achieved complete UMAP overlap, reflected in an ARI of 0.60 for slices merely 10μm apart (#151675 and #151676), and 0.58 for those 300μm apart.

For testing the methods with the horizontal slice integration, we used the anterior and posterior mouse brain slices. Unlike the methods SpaGCN and STAGATE that require pre-alignment of slice edges, STAIG without such prior spatial alignment precisely identified key brain structures such as cerebral cortex layers, cerebellum, and hippocampus, which aligns well with the annotation of Allen Brain Atlas (Fig. 5c) and shows accuracy comparable to the existing methods (Supplementary Fig. S11).

To further investigate the performances in partial overlap integration, we prepared the human placental bed dataset: three consecutive overlapped slices from a single donor, including Myometrium, Decidua, and Placenta, were segmented into 10 clusters[40]. Remarkably, STAIG seamlessly integrated the slices and eliminated the batch effects as shown in the UMAP plots (Fig. 5d). Especially, the slice 0 distinctively showing the domain 3, unique to the internal tissue of Myometrium. This distribution, exclusive to the slice 0 and absent in the slices 1 and 2. These results demonstrate that STAIG enables not only assimilating overlapped regions but also maintaining distinct characteristics of unique spatial regions.

Specifying the tumor microenvironment from human breast cancer ST

In the analysis of the human breast cancer dataset, we found that the results of STAIG closely matched the manual annotations and achieved the highest ARI of 0.64 (Supplementary Fig. S12). Notably, STAIG proposed a slightly different yet more refined spatial stratification. In particular, for the region 'Healthy_1' in the manual annotation (Fig. 6a), STAIG dissected it into subclusters Clusters 3 and 4 (Fig. 6b). We noticed that the differentially expressed genes (DEGs) in Cluster 3 compared with other clusters (>0.25 log2FoldChange, denotes as log2FC) (Fig. 6c) were significantly involved in biological processes, such as extracellular matrix organization, wound healing, and collagen fibril organization (Fig. 6d).

Interestingly, the DEGs included DCN, $CCL19$, and $CCL21$, which are well-known to function in cancer-associated fibroblasts (CAFs)[41,42]. Moreover, the CAF marker genes (e.g., $COL6A1$, $COL1A2$, *VIM*, *PDFGRB*, *S100A4*.)[43–45] were significantly upregulated in Cluster 3 (Fig. 6e) not in Cluster 4 (Supplementary Fig. S13a and S13b).

Taken together, through the integration of multi-modality by STAIG, we found that Cluster 3 shapes a tumor microenvironment densely populated by CAFs and unveiled the molecular property of CAF-rich area.

Identifying tumor-adjacent tissue junctions in zebrafish melanoma ST

To further characterize the tumor microenvironment, we investigated the A and B tissue slices of zebrafish melanoma (Fig. 7a): the previous study incorporated scRNA-seq data, thereby segmenting the interface clusters into muscle-like and tumor-like subclusters[46]. These clusters could not be specified by only the ST data analysis. Remarkably, STAIG identified the interfaces at the tumor-adjacent tissue junction using ST data only (Fig. 7b), which is often failed in the traditional ST methods (Supplementary Fig. S14, S15). In addition, the DEGs found from the interfaces included known genes, such as $si{:}dkey-153m14.1$, $zgc{:}158463$, $RPL41$, and $hspb9$ (Fig. 7c and Supplementary Fig. S16a), and were associated with mRNA metabolic processes (Fig. 7d and Supplementary Fig. S16b). These results highlight active transcriptional and translational processes in these regions, supporting the previous findings.

Subsequently, STAIG identified Cluster 12 in the slice A and Cluster 7 in the slice B as being closer to the tumor area, while Cluster 5 in the slice A and Cluster 9 in the slice B were positioned nearer to the muscle tissue. As shown in the UMAP plots (Fig. 7e), although Clusters 12 and 5 in the slice A were interconnected, Cluster 12 was aligned with tumor-associated clusters, and Cluster 5 was with normal tissue clusters. A similar pattern was observed with Clusters 7 and 9 in the slice B. Of note, the muscle-proximal subcluster showed a high expression of muscle marker genes[47,48], such as $atp2a1l$ and $ckma$ (Fig. 7f and Supplementary Fig. S16c-d), and the tumor-proximal subcluster exhibited a high expression of tumor-associated genes[49,50], e.g., $BRAF^{V600E}$ and $mt2$. These marker genes presented differential functional involvement (Supplementary Fig. S16e): the subcluster farther from the tumor showed an enrichment of muscle structure and metabolism, while that closer to the tumor was involved in protein folding and responding to temperature changes that are indicative of increased cellular activity and stress responses typically found in tumor cells[51].

In summary, we characterized the tumor borders of zebrafish melanoma and found that the cluster nearby tumors resembles a tumor-like interface, while the one closer to normal tissue is akin to a muscle-like interface. These results highlight the necessary of ST annotations and dissection in higher resolution to enhance the understanding of intricate cancer invasion.

Discussion

In this study, we proposed STAIG, a novel deep-leaning model that efficiently integrates gene expression, spatial coordinates, and histological images using graph contrastive learning coupled with a high-performance feature extraction. Unlike other methods, our approach first processed the images using Gaussian blurring and band-pass filtering which are essential in eliminating noise and enabling the model to focus on texture rather than color. Thereby, our model successfully extracted spatial features from a whole HE-stain image without relying on additional image data. These features were processed by the graph augmentation along with a unique contrastive loss function to focus on neighbor node consistency, which contributes to improving the performance of STAIG even in the setting without image data.

Furthermore, the contrastive integration of the augmented graphs focused on local node adjustments to facilitate dimensionality reduction and maintain node-to-neighbor relationships across different slices. This strategy allowed STAIG to process multiple slices together in an alignment-free manner by avoiding batch effects, as exemplified in the reconstructing of vertical, horizontal, and partially overlapped tissue slices. Note that this integration is most effective when applied to multiple tissue slices from the same source, which needs further work to overcome this limit.

By extensively benchmarking with various ST datasets, we demonstrated the effectiveness of STAIG by utilizing advanced image feature extraction if histological images are available. Remarkably, in the human breast cancer and zebrafish melanoma datasets, STAIG not only identified spatial regions in high resolution compared to the existing studies but also uncovered previously challenging-to-identify regions, offering unprecedented depth into tumor microenvironments. Additionally, STAIG showed exceptional capability in delineating tumor boundaries, outperforming others in identifying transitional zones with precision. This effectiveness is also linked to the contrast strategy of STAIG, which adeptly captures vital local information.

In conclusion, we confirmed the impact of combining advanced machine learning with multi-modal spatial information and

the promising potential of STAIG in deciphering cellular architectures, which facilitates our understanding of spatial biological intricates. As future works, since constructing a whole-graph representation is resource-intensive, especially on systems with limited GPU memory, it should be further considered how to optimize matrix compression during graph construction and how to effectively apply mini-batch approaches to optimize GNNs.

Methods

Data description

We downloaded publicly available ST datasets and histological images acquired from diverse platforms (see Supplementary Table S1). From the 10x Visium platform, the DLPFC dataset included 12 sections from three individuals, with each individual contributing four sections sampled at 10 μm and 300 μm intervals. The spot counts for these datasets varied between 3498 and 4789 per section, with the DLPFC dataset featuring annotations for its six layers and white matter. The human breast cancer dataset had 3798 spots, and the mouse brain dataset comprised anterior and posterior sections, with 2695 and 3355 spots respectively. For the zebrafish melanoma, two tissue slices A and B with 2179 and 2677 spots were analyzed. The human placental bed dataset included three consecutive slices from a single donor, with 3568, 3855, and 4186 spots per each. For integration experiments, the DLPFC, mouse brain, and human placental bed datasets were used.

The Stereo-seq dataset of the mouse olfactory bulb included 19109 spots with a 14μm resolution. Slide-seqV2 datasets featured a 10μm resolution with the mouse hippocampus (18765 spots from the central quarter radius) and the mouse olfactory bulb (19285 spots). The STARmap dataset comprised 1207 spots. These datasets lack images, and the image annotations were downloaded from the Allen Brain Atlas website (Supplementary Table S2).

Data preprocessing

Raw gene expression counts underwent log-transformation and normalization utilizing the SCANPY[52] package. Post-normalization, the data was scaled to achieve a mean of zero and unit variance. For our experiments, we selected a subset of F highly variable genes (HVGs), with F designated as 3000.

Basic graph construction

For each slice, we constructed a basic undirected neighborhood graph, $G = (V, E)$, where V represents the set of N spots $\{v_1, v_2, \dots v_N\}$, and $E \subseteq V \times V$ denotes the edges between these spots. The corresponding adjacency matrix, $A \in \{0,1\}^{N \times N}$, is defined such that $A_{ij} = 1$ indicates the presence of an edge $(v_i, v_j) \in E$. We determined the edges by computing a distance matrix $D \in \mathbb{R}^{N \times N}$, with D_{ij} representing the Euclidean distance between any two spots v_i and v_j. The KNN was employed to connect each spot with its top k closest spots, forming neighboring nodes. The gene expression matrix $X \in \mathbb{R}^{N \times F}$ was also established, where each row corresponds to the expression profile of HVGs for each spot.

Histological image feature extraction

For ST data with HE-stained slices, extracting image features from each spot was critical. We started with Gaussian blurring of the entire HE-stained image to reduce texture noise and staining biases. Next, 512×512 pixel patches centered on spot coordinates were extracted. These N patches underwent a band-pass filter to highlight cellular nuclear morphology.

We then utilized BYOL[18] for advanced self-supervised image feature extraction. In BYOL, images were resized to 224×224 pixels and underwent two random augmentations, including horizontal flipping, color distortion, Gaussian blurring, and solarization. These images were fed into two networks: the online network (comprising an encoder, a projector, and a predictor) and the target network (similar but without the predictor). Both networks used the ResNet[53] architecture for encoding and multi-layer perceptrons for projecting and predicting. Embeddings from these networks were synchronized using an $L2$ loss for consistency.

Post-training, the encoder of the target network produced a 2048-dimensional feature vector for each image, reduced to 64 components via Principal Component Analysis[54]. The resulting matrix $C \in \mathbb{R}^{N \times 64}$ represented the image features, with each

row c_i corresponding to the features of spot v_i.

Integration of slices

When dealing with multiple consecutive tissue slices, each slice was processed individually. Given m slices, with the respective number of spots $N_1, N_2, \dots, N_m$, the total spot count T was the sum of all N_i. We then had distinct adjacency matrices A^1 to A^m and image feature matrices C^1 to C^m for each slice. Batch integration commenced with the vertical concatenation of raw gene expressions into a single matrix, which was then normalized to a mean of zero and scaled for unit variance. From this, F HVGs were selected, forming the integrated expression matrix $\mathcal{X} \in \mathbb{R}^{T \times F}$.

For next step, we must integrate these matrices. Adjacency matrices were combined into a block-diagonal matrix $\mathcal{A}$, as shown in Equation (1), and image feature matrices were vertically concatenated to form matrix $\mathcal{C}$, as per Equation (2). These integrated matrices became the basis for further analysis.

$$\mathcal{A} = \begin{bmatrix} A^1 & \cdots & 0 \\ \vdots & \ddots & \vdots \\ 0 & \cdots & A^m \end{bmatrix} \in \mathbb{R}^{T \times T} \tag{1}$$

$$\mathcal{C} = \begin{bmatrix} C^1 \\ \vdots \\ C^m \end{bmatrix} \in \mathbb{R}^{T \times 64} \tag{2}$$

Graph augmentation

The contrastive learning workflow in STAIG was based on the GCA framework[55]. Each iteration augmented the input graph, resulting in two modified graphs, G^1 and G^2, as well as their associated gene expression matrices, $\mathcal{X}^1$ and $\mathcal{X}^2$. These were derived from the original graph G, which possessed an edge set $\mathcal{E}$, through a specific augmentation strategy applied to the integrated adjacency matrix $\mathcal{A}$ and the gene expression matrix $\mathcal{X}$.

Utilizing the integrated image feature matrix $\mathcal{C}$, we computed the image spatial distance matrix $D^{img} \in R^{T \times T}$, with D_{ij}^{img} indicating the Euclidean distance between spots v_i and v_j in the image feature space. The edge weight matrix W was defined by combining $\mathcal{A}$ with D^{img}, followed by a logarithmic transformation to modulate the distance values, as depicted in Equation (3):

$$W = \mathcal{A} \odot log\left(D^{img} + 1\right), \tag{3}$$

The symbol $\odot$ represented the element-wise multiplication, and the addition of 1 prevented the logarithm of zero.

W was then scaled to a probability matrix $P \in \mathbb{R}^{T \times T}$ by the SoftMax function, with each element $P_{i,j}$ being calculated as per Equation (4):

$$P_{i,j} = \begin{cases} \dfrac{e^{W_{i,j}}}{\sum_{k=1}^{T} e^{W_{i,k}} \mathcal{A}_{i,k}}, & if\ \mathcal{A}_{i,j} = 1 \\ 0, & otherwise \end{cases} \tag{4}$$

During each iteration, the augmented graphs G^1 and G^2 maintained the node set V of original graph G. However, their sets of edges, $\mathcal{E}^1$ and $\mathcal{E}^2$ were independently formed by probabilistically removing each edge from $\mathcal{E}$ (for example, an edge $(v_i, v_j) \in \mathcal{E}$), based on the probability p_{ij}^e, derived from P and adjusted within a range set by p_{min} and p_{max} as in Equation (5).

$$p_{ij}^e = p_{min} + (p_{max} - p_{min}) \times P_{i,j}, \tag{5}$$

Here, p_{min} served as the minimum probability for an edge to be considered for removal. The thresholds for p_{min} and p_{max} were set as per Equation (6).

$$0 < p_{min} < p_{max} < 1 \tag{6}$$

In scenarios lacking image data, STAIG defaulted to a fixed edge removal probability of 0.3.

The gene expression matrix $\mathcal{X}$ was augmented by introducing variability like salt-and-pepper noise in images. This involved two independent random vectors r^1 and r^2, each within $\{0,1\}^F$. These elements in vectors were sampled

from a Bernoulli distribution. The augmented matrices $\mathcal{X}^1$ and $\mathcal{X}^2$ were then formulated by multiplying each row x_i in $\mathcal{X}$ with r^1 and r^2 respectively, as described in Equation (7):

$$x_i^1 = r^1 \odot x_i, \qquad x_i^2 = r^2 \odot x_i \tag{7}$$

Here, x_i^1 and x_i^2 corresponded to the respective rows in $\mathcal{X}^1$ and $\mathcal{X}^2$.

Contrastive learning in the STAIG framework based on the GCA architecture

In every iteration, G^1 and G^2 were processed through a shared GNN, structured with l layers of GCNs followed by two layers of fully connected network, yielding embeddings H^1 and H^2 for each graph as follows:

$$H^1 = GNN\left(G^1, \mathcal{X}^1\right) \in \mathbb{R}^{T\times F'}, \qquad H^2 = GNN\left(G^2, \mathcal{X}^2\right) \in \mathbb{R}^{T\times F'}, \tag{8}$$

where $F' \ll F$, and the rows h_i^1 and h_i^2 in H^1 and H^2 represented the embeddings of spot v_i in the augmented graphs G^1 and G^2, respectively.

In the STAIG model, a neighbor contrastive learning loss[56] was employed to ensure the consistency and distinctiveness of embeddings in H^1 and H^2. This involved constructing and comparing positive and negative sample pairs.

For the positive pairs, we considered the embedding $h_i^{(1)}$ of v_i in G^1 as the example. Positive pairs were sourced from: **(1)** The embedding $h_i^{(2)}$ of the same spot v_i in G^2; **(2)** embeddings of neighboring nodes of v_i in G^1, denoted as $h_j^{(1)}|v_j \in \mathcal{N}_i^1$, where $\mathcal{N}_i^1$ represented the set of neighboring nodes of v_i in G^1; and **(3)** embeddings of neighboring nodes of v_i in G^2, expressed as $h_j^{(2)}|v_j \in \mathcal{N}_i^2$, with $\mathcal{N}_i^2$ being the set of neighbors of v_i in G^2. The total number of positive pairs for the anchor $h_i^{(1)}$ was $\widehat{\mathcal{N}_i} = \left|\mathcal{N}_i^1\right| + \left|\mathcal{N}_i^2\right| + 1$, where $\left|\mathcal{N}_i^1\right|$ and $\left|\mathcal{N}_i^2\right|$ denoted the counts of neighboring nodes of v_i in G_1 and G_2, respectively.

In contrast, negative sample pairs were generally defined as all pairs other than the positive ones. However, selecting negative samples without considering class information led to 'sampling bias'[19], where many negative samples were incorrectly classified as belonging to the same class. This negatively impacted clustering results. To address this issue, when images are available ,we implemented the DS[19]. DS filtered out false negatives based on the similarity of image features c_i of each spot v_i. Initially, spots were clustered into Q classes using the K-means method based on their image features, creating pseudo labels $Y_p = \{y_i\}_{i=1}^T$. During the construction of negative samples, any v_i sharing the same pseudo label was excluded.

The neighbor contrastive loss associated with the anchor $h_i^{(1)}$ between G^1 and G^2 was given by:

$$l\left(h_i^{(1)}\right) = -log\frac{\left(f^{1,2}(i,i) + \sum_{v_j\in\mathcal{N}_i^1} f^{1,1}(i,j) + \sum_{v_j\in\mathcal{N}_i^2} f^{1,2}(i,j)\right)/\widehat{\mathcal{N}_i}}{f^{1,2}(i,i) + \sum_{(j\neq i)\cap\left(y_j\neq y_i\right)}\left(f^{1,1}(i,j) + f^{1,2}(i,j)\right)}, \tag{9}$$

here, $f^{1,1}(i,j) = e^{\theta\left(h_i^{(1)},h_j^{(1)}\right)/\tau}$, $f^{1,2}(i,j) = e^{\theta\left(h_i^{(1)},h_j^{(2)}\right)/\tau}$, τ was a temperature parameter, and $\theta(\cdot)$ represented a similarity measure (in our work, the inner product is employed). Given the structural similarity between G^1 and G^2, the computation for $l\left(h_i^{(2)}\right)$ mirrored that of $l\left(h_i^{(1)}\right)$. The final neighbor contrastive loss, averaged over both augmented graphs, was expressed as:

$$l\left(H^1, H^2\right) = \frac{1}{2T}\sum_{i=1}^{T}\left[l\left(h_i^{(1)}\right) + l\left(h_i^{(2)}\right)\right] \tag{10}$$

Spatial domain identification through clustering and refinement

Upon the completion of training, the spot embeddings in both augmented graphs were averaged to derive the final low-dimensional representation H given as follows:

$$H = \frac{1}{2}(H^1 + H^2) \tag{11}$$

The H was clustered using the mclust[57] algorithm, which was based on a Gaussian Mixture Model. For datasets that come with manual annotations, the number of clusters was set to match the number of labeled classes. In the absence of such annotations, the SC determined the number of clusters, with the count corresponding to the highest SC designated as the final number for the spatial domain.

Consistent with previous baseline methods, we employed a refinement technique for the DLPFC dataset[20] to further mitigate noise, ensuring a smoother delineation of clustering boundaries. As part of this refinement, for a given v_i, all spots within a radius d in its spatial vicinity were assigned the same class as v_i.

Regarding multi-slice integration, since all data has been amalgamated into a single matrix prior to model input, the embeddings of spots across different slices outputted by the GNN have already had batch differences eliminated. The procedure for spatial identification mirrored that for single-slice processing.

The overall architecture of STAIG

The architecture of STAIG featured a GNN with one GCN layer and two layers of fully connected network, outputting a 64-dimensional F'. It employed a 'Parametric Rectified Linear Unit' activation function and used the Adam optimizer with an initial learning rate of 5×10^{-4} and a weight decay of 1×10^{-5}. The model ran for 400 epochs, with a temperature parameter τ set to 10 and a neighbor count k of 5 by default. Further details on hyperparameter optimization can be found in the 'Hyperparameter optimization' of the Supplementary Information.

The ablation studies of STAIG

To assess the effectiveness of STAIG solely on its novel contrastive learning framework and the efficacy of graph augmentation strategy utilizing image information, we conducted ablation experiments on the DLPFC dataset. The experimental setup included: the basic framework without image data, using DS (fixed graph edge removal probability) with image data, employing only adaptive edge random removal based on image features, and the complete framework implementation.

The results demonstrated the consistent of STAIG superiority in median ARI compared to other methods, even in the absence of image data. Both the adaptive random edge removal strategy and the DS grounded in the significantly improved the average and median ARI values. Comprehensive details of these ablation studies are provided in the 'Ablation studies' of the Supplementary Information.

Visualization and functional analysis of spatial domain

The spatial domains detected were visualized using UMAP. The differential gene expression was analyzed using the Wilcoxon test of SCANPY. The Gene ontology analysis was done by clusterProfiler[58]. For differential expressed gene analysis, $|\log2FC| > 0.25$ and p-value < 0.05 were used as the marker gene selection threshold. The p-values were calculated by Wilcoxon Rank Sum test.

Declarations

Ethics approval and consent to participate

Not applicable.

Consent for publication

Not applicable.

Competing interests

Not applicable.

Funding

XXXX

Authors' contributions

Y.Y. and K.N. conceived and designed the study. Y.Y. and Y.C. performed data analysis. Y.Y., Y.C. and K.N. drafted the manuscript. S.P., M.L., X.Z., and Y.Z. provided guidance on data analysis. All the authors have read and approved the final version of manuscript.

Acknowledgements

Computational resource was provided by the supercomputer system SHIROKANE at Human Genome Center, the Institute of Medical Science, the University of Tokyo.

Data availability

The data sets examined in our research can be accessed in their unprocessed state directly from the creators, as detailed in Supplementary Tables S1 and S2. Additionally, the data utilized for this study is now openly accessible on Zenodo at the following link: https://zenodo.org/records/10277128.

Code availability

The source code for STAIG is openly available for academic and non-commercial use. It can be accessed at the following GitHub repository: https://github.com/y-itao/STAIG. This repository includes all necessary instructions for installation, usage, and a detailed README for guidance.

Reference

1. Rao, N., Clark, S. & Habern, O. Bridging Genomics and Tissue Pathology: 10x Genomics explores new frontiers with the Visium Spatial Gene Expression Solution. *Genetic Engineering & Biotechnology News* **40**, 50–51 (2020).
2. Rodriques, S. G. *et al.* Slide-seq: A scalable technology for measuring genome-wide expression at high spatial resolution. *Science* **363**, 1463–1467 (2019).
3. Chen, A. *et al.* Spatiotemporal transcriptomic atlas of mouse organogenesis using DNA nanoball-patterned arrays. *Cell* **185**, 1777-1792.e21 (2022).
4. Wang, X. *et al.* Three-dimensional intact-tissue sequencing of single-cell transcriptional states. *Science* **361**, eaat5691 (2018).
5. Dries, R. *et al.* Advances in spatial transcriptomic data analysis. *Genome Res.* **31**, 1706–1718 (2021).
6. Hartigan, J. A. & Wong, M. A. Algorithm AS 136: A K-Means Clustering Algorithm. *Applied Statistics* **28**, 100 (1979).
7. Traag, V. A., Waltman, L. & Van Eck, N. J. From Louvain to Leiden: guaranteeing well-connected communities. *Sci Rep* **9**, 5233 (2019).
8. Hao, Y. *et al.* Integrated analysis of multimodal single-cell data. *Cell* **184**, 3573-3587.e29 (2021).
9. Zhao, E. *et al.* Spatial transcriptomics at subspot resolution with BayesSpace. *Nat Biotechnol* **39**, 1375–1384 (2021).
10. Fu, H. *et al. Unsupervised Spatially Embedded Deep Representation of Spatial Transcriptomics*. http://biorxiv.org/lookup/doi/10.1101/2021.06.15.448542 (2021) doi:10.1101/2021.06.15.448542.
11. Dong, K. & Zhang, S. Deciphering spatial domains from spatially resolved transcriptomics with an

adaptive graph attention auto-encoder. *Nat Commun* **13**, 1739 (2022).
12. Long, Y. *et al.* Spatially informed clustering, integration, and deconvolution of spatial transcriptomics with GraphST. *Nat Commun* **14**, 1155 (2023).
13. Pham, D. *et al. stLearn: integrating spatial location, tissue morphology and gene expression to find cell types, cell-cell interactions and spatial trajectories within undissociated tissues*. http://biorxiv.org/lookup/doi/10.1101/2020.05.31.125658 (2020) doi:10.1101/2020.05.31.125658.
14. Hu, J. *et al.* SpaGCN: Integrating gene expression, spatial location and histology to identify spatial domains and spatially variable genes by graph convolutional network. *Nat Methods* **18**, 1342–1351 (2021).
15. Xu, C. *et al.* DeepST: identifying spatial domains in spatial transcriptomics by deep learning. *Nucleic Acids Research* **50**, e131–e131 (2022).
16. Zong, Y. *et al. conST: an interpretable multi-modal contrastive learning framework for spatial transcriptomics*. http://biorxiv.org/lookup/doi/10.1101/2022.01.14.476408 (2022) doi:10.1101/2022.01.14.476408.
17. He, K. *et al.* Masked Autoencoders Are Scalable Vision Learners. in *2022 IEEE/CVF Conference on Computer Vision and Pattern Recognition (CVPR)* 15979–15988 (IEEE, 2022). doi:10.1109/CVPR52688.2022.01553.
18. Grill, J.-B. *et al.* Bootstrap Your Own Latent a New Approach to Self-Supervised Learning. in *Proceedings of the 34th International Conference on Neural Information Processing Systems* (Curran Associates Inc., 2020).
19. Zhao, H., Yang, X., Wang, Z., Yang, E. & Deng, C. Graph Debiased Contrastive Learning with Joint Representation Clustering. in *Proceedings of the Thirtieth International Joint Conference on Artificial Intelligence* 3434–3440 (International Joint Conferences on Artificial Intelligence Organization, 2021). doi:10.24963/ijcai.2021/473.
20. Maynard, K. R. *et al.* Transcriptome-scale spatial gene expression in the human dorsolateral prefrontal cortex. *Nat Neurosci* **24**, 425–436 (2021).
21. Steinley, D. Properties of the hubert-arable adjusted rand index. *Psychological methods* **9**, 386 (2004).
22. Shahapure, K. R. & Nicholas, C. Cluster quality analysis using silhouette score. in *2020 IEEE 7th international conference on data science and advanced analytics (DSAA)* 747–748 (IEEE, 2020).
23. Long, Y. *et al.* Spatially informed clustering, integration, and deconvolution of spatial transcriptomics with GraphST. *Nat Commun* **14**, 1155 (2023).
24. Dong, K. & Zhang, S. Deciphering spatial domains from spatially resolved transcriptomics with an adaptive graph attention auto-encoder. *Nat Commun* **13**, 1739 (2022).
25. Xu, C. *et al.* DeepST: identifying spatial domains in spatial transcriptomics by deep learning. *Nucleic Acids Research* **50**, e131–e131 (2022).
26. Lein, E. S. *et al.* Genome-wide atlas of gene expression in the adult mouse brain. *Nature* **445**, 168–176 (2007).
27. Keller, J. M., Gray, M. R. & Givens, J. A. A fuzzy K-nearest neighbor algorithm. *IEEE Trans. Syst., Man, Cybern.* **SMC-15**, 580–585 (1985).
28. Seroogy, K. B., Brecha, N. & Gall, C. Distribution of cholecystokinin-like immunoreactivity in the rat main olfactory bulb. *J of Comparative Neurology* **239**, 373–383 (1985).
29. Farmer, W. T. & Murai, K. Resolving Astrocyte Heterogeneity in the CNS. *Front. Cell. Neurosci.* **11**, 300 (2017).
30. Deans, M. R. *et al.* Control of Neuronal Morphology by the Atypical Cadherin Fat3. *Neuron* **71**, 820–832 (2011).
31. Paul, A., Chaker, Z. & Doetsch, F. Hypothalamic regulation of regionally distinct adult neural stem cells and neurogenesis. *Science* **356**, 1383–1386 (2017).
32. Tabar, V. *et al.* Migration and differentiation of neural precursors derived from human embryonic stem cells in the rat brain. *Nat Biotechnol* **23**, 601–606 (2005).
33. Mamoor, S. *The α1 subunit of the γ-aminobutyric acid receptor, Gabra1, is differentially expressed in*

the brains of patients with schizophrenia. https://osf.io/m93ya (2020) doi:10.31219/osf.io/m93ya.
34. Stickels, R. R. *et al.* Highly sensitive spatial transcriptomics at near-cellular resolution with Slide-seqV2. *Nat Biotechnol* **39**, 313–319 (2021).
35. Biesemann, C. *et al.* Proteomic screening of glutamatergic mouse brain synaptosomes isolated by fluorescence activated sorting. *EMBO J* **33**, 157–170 (2014).
36. Calì, T., Brini, M. & Carafoli, E. The PMCA pumps in genetically determined neuronal pathologies. *Neuroscience Letters* **663**, 2–11 (2018).
37. Iijima, T., Miura, E., Watanabe, M. & Yuzaki, M. Distinct expression of C1q-like family mRNAs in mouse brain and biochemical characterization of their encoded proteins. *Eur J of Neuroscience* **31**, 1606–1615 (2010).
38. Takeda, K. WFS1 (Wolfram syndrome 1) gene product: predominant subcellular localization to endoplasmic reticulum in cultured cells and neuronal expression in rat brain. *Human Molecular Genetics* **10**, 477–484 (2001).
39. Newrzella, D. *et al.* The functional genome of CA1 and CA3 neurons under native conditions and in response to ischemia. *BMC Genomics* **8**, 370 (2007).
40. Arutyunyan, A. *et al.* Spatial multiomics map of trophoblast development in early pregnancy. *Nature* **616**, 143–151 (2023).
41. Bockstal, M. V. *et al.* Differential regulation of extracellular matrix protein expression in carcinoma-associated fibroblasts by TGF-β1 regulates cancer cell spreading but not adhesion. *Oncoscience* **1**, 634–648 (2014).
42. Ozga, A. J., Chow, M. T. & Luster, A. D. Chemokines and the immune response to cancer. *Immunity* **54**, 859–874 (2021).
43. Han, C., Liu, T. & Yin, R. Biomarkers for cancer-associated fibroblasts. *Biomark Res* **8**, 64 (2020).
44. Zhang, H. *et al.* Define cancer-associated fibroblasts (CAFs) in the tumor microenvironment: new opportunities in cancer immunotherapy and advances in clinical trials. *Mol Cancer* **22**, 159 (2023).
45. Kay, E. J. *et al.* Cancer-associated fibroblasts require proline synthesis by PYCR1 for the deposition of pro-tumorigenic extracellular matrix. *Nat Metab* **4**, 693–710 (2022).
46. Hunter, M. V., Moncada, R., Weiss, J. M., Yanai, I. & White, R. M. Spatially resolved transcriptomics reveals the architecture of the tumor-microenvironment interface. *Nat Commun* **12**, 6278 (2021).
47. Jin, S. *et al.* Ebf factors and MyoD cooperate to regulate muscle relaxation via Atp2a1. *Nat Commun* **5**, 3793 (2014).
48. Bayir, M., Arslan, G. & Oğuzhan Yildiz, P. Characterization, Identification and Phylogeny of the Creatine Kinase (ckma) Gene in Medaka (Oryzias latipes). *Marine Science and Technology Bulletin* **9**, 15–22 (2020).
49. Ascierto, P. A. *et al.* The role of BRAF V600 mutation in melanoma. *J Transl Med* **10**, 85 (2012).
50. OHNISHI, Y., TAJIMA, S. & ISHIBASHI, A. Coordinate expression of membrane type-matrix metalloproteinases-2 and 3 (MT2-MMP and MT3-MMP) and matrix metalloproteinase-2 (MMP-2) in primary and metastatic melanoma cells. *European Journal of Dermatology* **11**, 420–3 (2001).
51. Wang, M., Law, M. E., Castellano, R. K. & Law, B. K. The unfolded protein response as a target for anticancer therapeutics. *Critical Reviews in Oncology/Hematology* **127**, 66–79 (2018).
52. Wolf, F. A., Angerer, P. & Theis, F. J. SCANPY: large-scale single-cell gene expression data analysis. *Genome Biol* **19**, 15 (2018).
53. Wu, Z., Shen, C. & Van Den Hengel, A. Wider or Deeper: Revisiting the ResNet Model for Visual Recognition. *Pattern Recognition* **90**, 119–133 (2019).
54. Wold, S., Esbensen, K. & Geladi, P. Principal component analysis. *Chemometrics and intelligent laboratory systems* **2**, 37–52 (1987).
55. Zhu, Y. *et al.* Graph Contrastive Learning with Adaptive Augmentation. in *Proceedings of the Web Conference 2021* 2069–2080 (ACM, 2021). doi:10.1145/3442381.3449802.
56. Shen, X., Sun, D., Pan, S., Zhou, X. & Yang, L. T. Neighbor Contrastive Learning on Learnable Graph

Augmentation. *AAAI* **37**, 9782–9791 (2023).
57. Scrucca, L., Fop, M., Murphy, T. B. & Raftery, A. E. mclust 5: clustering, classification and density estimation using Gaussian finite mixture models. *The R journal* **8**, 289 (2016).
58. Yu, G., Wang, L.-G., Han, Y. & He, Q.-Y. clusterProfiler: an R Package for Comparing Biological Themes Among Gene Clusters. *OMICS: A Journal of Integrative Biology* **16**, 284–287 (2012).

Fig. 1 Overview of the STAIG framework. (**a**) STAIG begins with spatial transcriptomic (ST) data. Each slice includes spots with spatial coordinates, gene data, and optional Hematoxylin and Eosin (HE) stained images. Image patches at these spots undergo noise reduction, including bandpass filtering, before being processed for image embeddings via the BYOL framework. Parallelly, an adjacency matrix is created using the spatial data of the spots. (**b**) For multiple slices, the image embeddings from each slice are vertically merged, forming an image embedding space where spots are distributed, with dotted lines indicating their Euclidean distances. (**c**) Adjacency matrices from each section are combined diagonally to form an integrated adjacency matrix. This matrix is then used to construct a graph, with gene expression data represented as node information. (**d**) For spots connected by edges, distances are calculated in the image embedding space. These distances are then transformed into probabilities of random edge removal using a SoftMax function. The original graph undergoes two rounds of edge random removal based on these probabilities, creating two augmented views. Subsequently, features of nodes in these graph views are randomly masked. (**e**) A graph neural network (GNN) processes these augmented views, concentrating on node-level differences. This step is encapsulated within a dotted box, emphasizing the neighbor contrastive strategy. (**f**) The derived embeddings from the GNN are then utilized for spatial domain identification and integration.

Fig. 2 Enhanced spatial region identification in Human Dorsolateral Prefrontal Cortex (DLPFC) and mouse brain tissues by STAIG. (a) Boxplots of adjusted rand index (ARI) of the nine methods applied to all 12 DLPFC slices. In the boxplot, the center line denotes the median, box limits denote the upper and lower quartiles, black dots denote individual slice, and whiskers denote the 1.5× interquartile range. **(b)** Manual annotations and clustering results with ARI by STAIG on DLPFC slice #151672. **(c)** Manual annotations, HE stained image, clustering result with ARI and UMAP visualization by STAIG on DLPFC slice #151673. **(d)** UMAP visualizations by baseline methods (stLearn, Seurat, STAGATE, SpaGCN, DeepST, conST, SEDR, GraphST) on DLPFC slice #151673. **(e)** Clustering results with ARI by baseline methods on DLPFC slice #151673. Manual annotations and clustering results of the other DLPFC slices are shown in Supplementary Fig. S1 and S2. **(f)** HE stained image, anatomical annotations from the Allen Reference Atlas, and clustering results with Silhouette Coefficient (SC) by STAIG on mouse brain posterior tissue. The red box denotes the cerebellar cortex, and the yellow box denotes hippocampal area with Ammon's horn (CA) and Dentate Gyrus (DG). Clustering results from baseline methods are shown in Supplementary Fig. S3. **(g)** Manual annotations from Long et al. and bar charts of ARI by STAIG and baseline methods on mouse anterior tissue. The y-axis represents ARI. Clustering results from baseline methods are shown in Supplementary Fig. S4.

Fig. 3 Improving spatial transcriptomic analysis through advanced image feature extraction in STAIG. (a) HE stained image, manual annotations and KNN clustering results based purely on image features by STAIG and three other image-based methods (stLearn, DeepST, ConST) on DLPFC slice #151507. **(b)** HE stained image, manual annotations and KNN clustering results based purely on image features by STAIG and three other image-based methods on DLPFC slice #151673. **(c)** HE stained image, visual interpretation based manual annotations and KNN clustering results based purely on image features by STAIG and three other image-based methods on human breast cancer dataset.

Fig. 4 Robust performance of STAIG in spatial transcriptomics lacking image data.
(**a**) DAPI-stained image with annotated laminar organization and clustering results with SC by STAIG, STAGATE, GraphST, and Seurat on Stereo-seq mouse olfactory bulb tissue. Clustering results from other baseline methods are shown in Supplementary Fig. S5. (**b**) Visualization of spatial domains identified by STAIG and the corresponding marker gene expressions on the Stereo-seq mouse olfactory bulb tissue. (**c**) Bar chart of SC by STAIG and baseline methods on Stereo-seq mouse olfactory bulb tissue. The y-axis represents SC. (**d**) Annotations from the Allen Reference Atlas and clustering results with SC by STAIG on Slide-seqV2 mouse olfactory bulb tissue. Clustering results from baseline methods are shown in

Supplementary Fig. S6. (**e**) Bar chart of SC by STAIG and baseline methods on Slide-seqV2 mouse olfactory bulb tissue. The x-axis represents SC. (**f**) Annotations from the Allen Reference Atlas, clustering results with SC and visualization of CA1, CA3 and DG domains identified by STAIG and the corresponding marker gene expressions on Slide-seqV2 mouse hippocampus tissue. Clustering results from baseline methods are shown in Supplementary Fig. S7. (**g**) Manual annotations and clustering results with ARI by STAIG, STAGATE, GraphST, and Seurat on STARmap mouse visual cortex dataset. Clustering results from other baseline methods are shown in Supplementary Fig. S8.

Fig. 5 Integration Capabilities of STAIG. (a) Vertical integration of STAIG at 10μm (DLPFC slice #151675 and #151676). Includes a simplified slice sampling diagram, manual annotations, integrated UMAP, and ARI. Baseline methods results detailed in Supplementary Figure S9. **(b)** Vertical integration of STAIG at 300μm (DLPFC slice #151508 and #151509). Includes a simplified slice sampling diagram, manual annotations, integrated UMAP, and ARI. Baseline methods results detailed in Supplementary Fig. S10. (**c**) Horizontal integration of STAIG. Includes HE stained images, annotations from the Allen Reference Atlas and integration results by STAIG on mouse anterior and posterior brain tissue slices. The red box highlights the hippocampus zones in both slices. Baseline methods results are shown in Supplementary Fig. S11. (**d**) Partial overlap integration of STAIG. HE stained images and integration results with UMAP visualization by STAIG on three partially overlapping slices from the human placental bed dataset.

Fig. 6 Advanced spatial analysis by STAIG reveals Cancer-associated fibroblasts (CAF)-rich clusters in human Breast Cancer ST Data.

(**a**) Manual annotation of human breast cancer dataset based on the HE-stain image. (**b**) Clustering results with ARI by STAIG on human breast cancer dataset. Clustering results from other baseline methods are shown in Supplementary Fig. S12. (**c**) Differential Gene Expression (DGE) analysis of Cluster 3 versus other clusters. Each point represents a gene, the vertical axis represents the -log10 of the p-value and the horizontal axis represents the log2FoldChange (log2 FC). The significance threshold is set at $|\log2FC| > 0.25$. (**d**) Gene Ontology (GO) analysis for Cluster 3 versus other clusters. The vertical axis represents the GO terms, and the horizontal axis represents the -log10 of the p-value. (**e**) Violin plots and the visualization of expression of CAF marker genes ($COL6A1$, $COL1A2$, VIM, $PDGFRB$, $S100A4$) in Cluster 3 versus other clusters. The vertical axis represents gene expression levels. Each 'violin' represents the distribution of expression for a particular gene, with the width indicating frequency. The large box between pairs of violins shows the statistical comparison between Cluster 3 and other clusters. The presence of stars on this box denotes statistical significance, with the number of stars corresponding to the level of significance (e.g., $*p < 0.05$, $**p < 0.01$, $***p < 0.001$, $****p < 0.0001$).

Fig. 7 Enhanced resolution of tumor interface dynamics in zebrafish melanoma using STAIG analysis.

(**a**) HE stained image and annotation of zebrafish melanoma on slice A and B from Hunter et al. (2021). (**b**) Interface domains identified by STAIG on slice A and B with SC. Baseline methods results are shown in Supplementary Fig. S13 and S14. (**c**) DGE analysis of the interface domain versus other domains on slice A. (**d**) GO analysis for the identified interface domain versus other domains on slice A. (**e**) UMAP visualization of clustering results on slice A and B by STAIG. The red outline indicates clusters of normal tissue, while the blue outline denotes clusters of tumor tissue.

(**f**) Fine-tuned subregions (muscle-proximal and tumor-proximal) of the interface identified by STAIG and the gene expression patterns of specific genes ($atp2a1l$, $ckma$, $BRAF^{V600E}$, $mt2$).

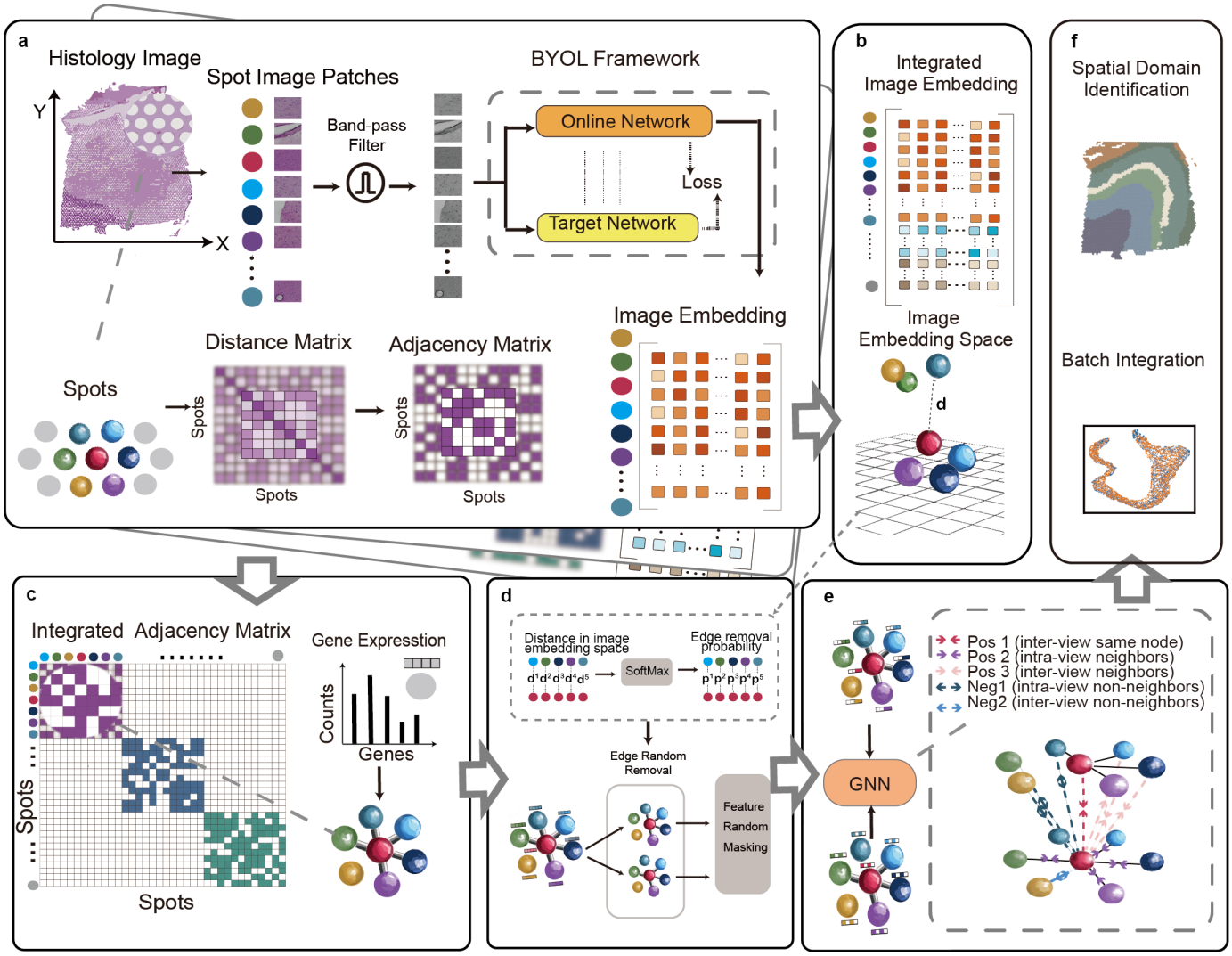

Fig. 1 Overview of the STAIG framework.

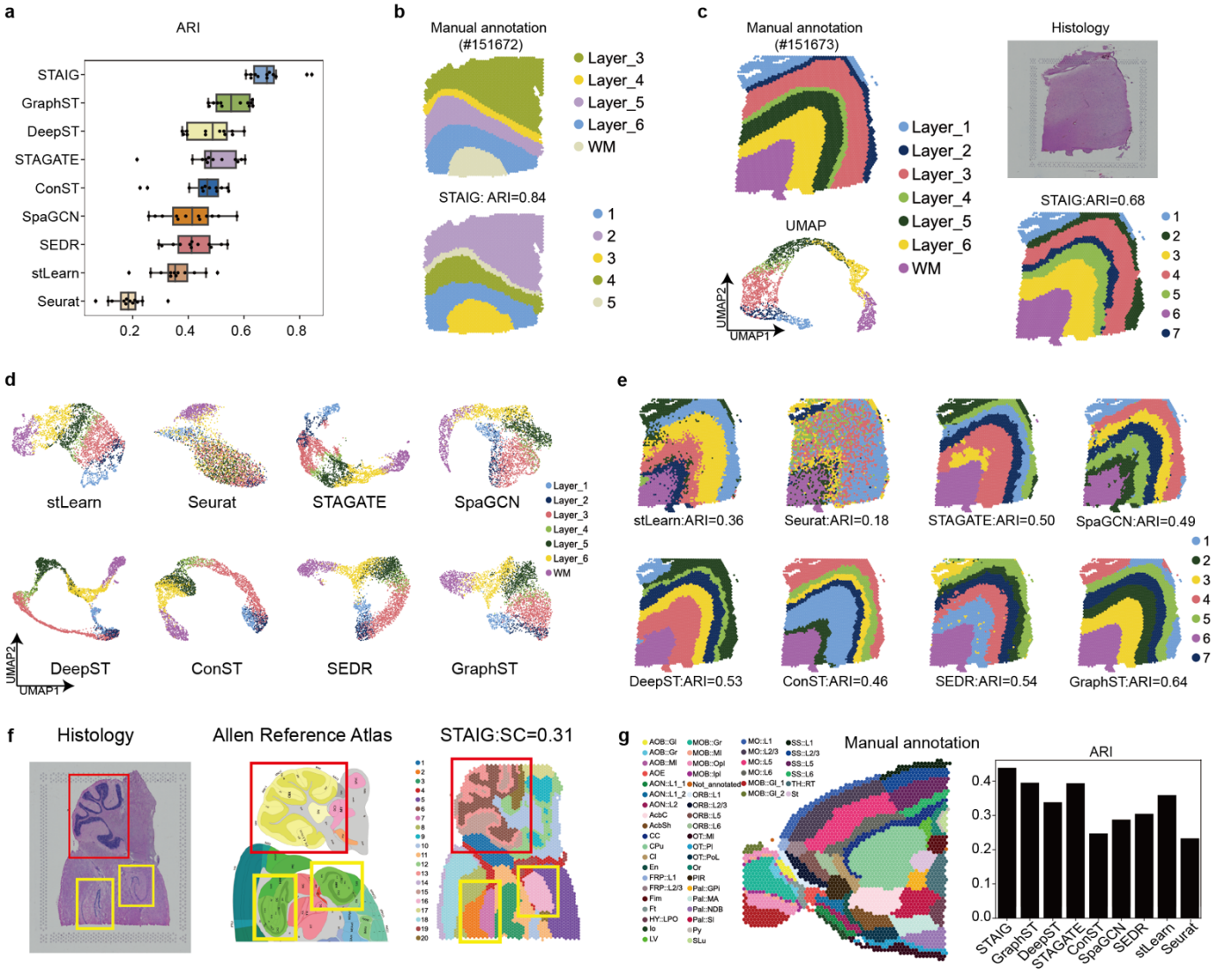

Fig. 2 Enhanced spatial region identification in Human Dorsolateral Prefrontal Cortex (DLPFC) and mouse brain tissues by STAIG.

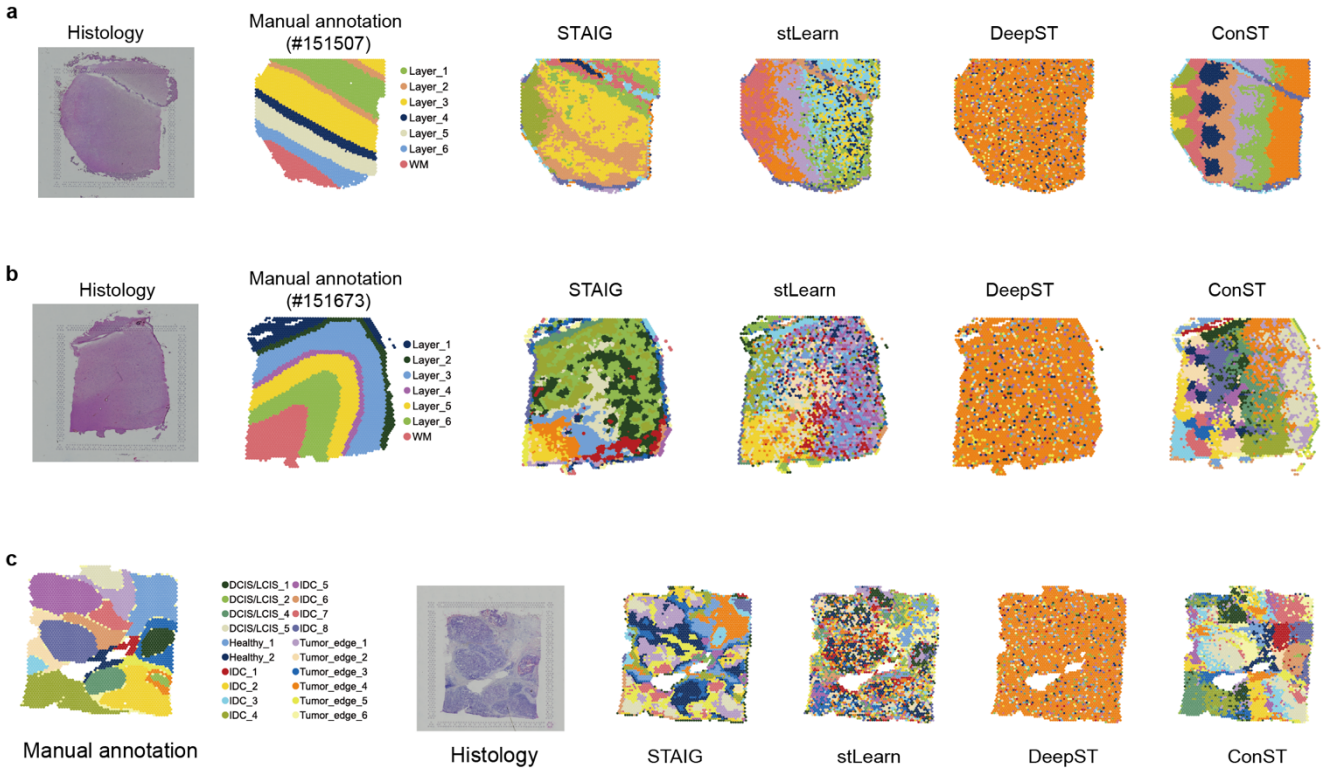

Fig. 3 Improving spatial transcriptomic analysis through advanced image feature extraction in STAIG.

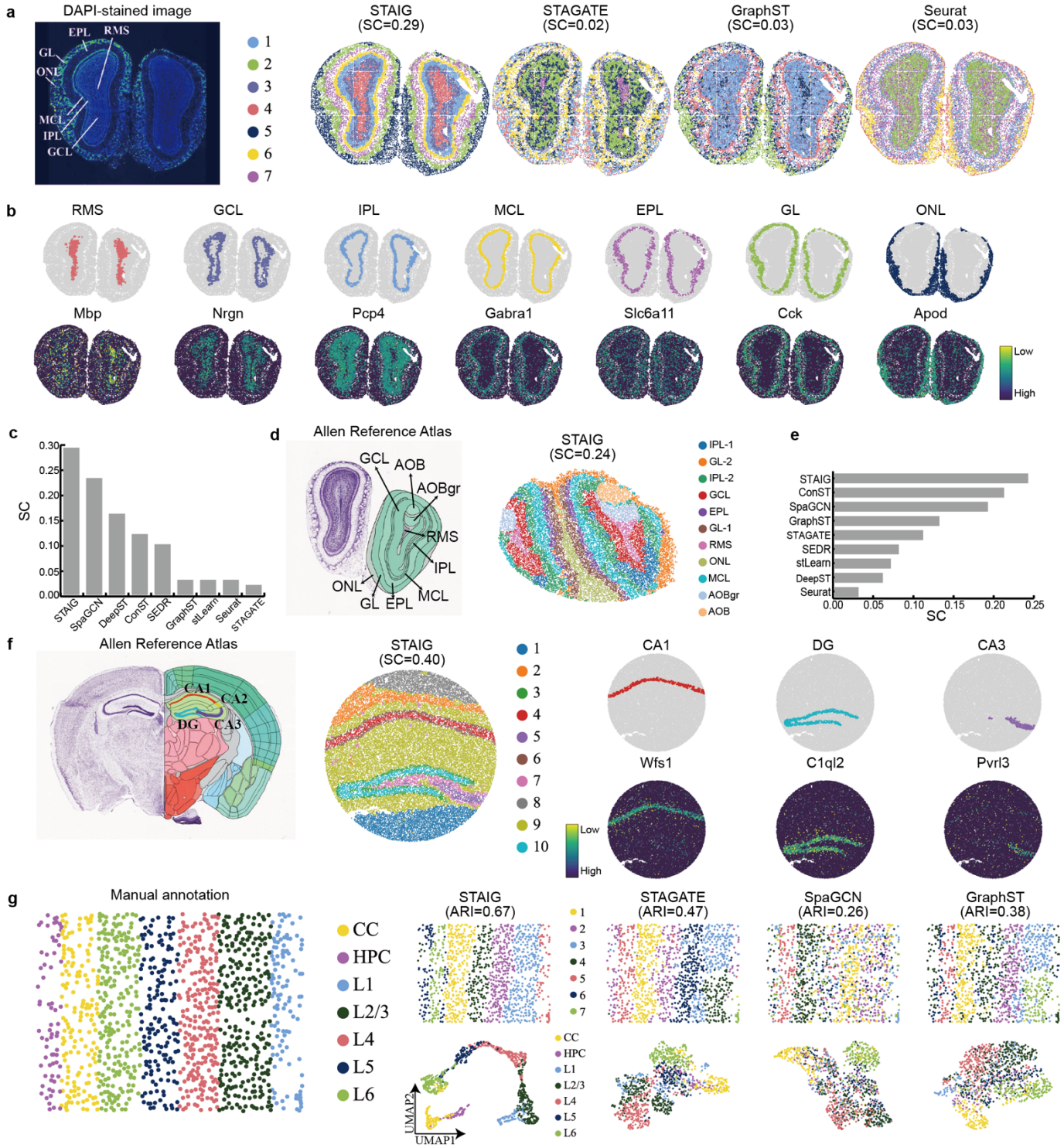

Fig. 4 Robust performance of STAIG in spatial transcriptomics lacking image data.

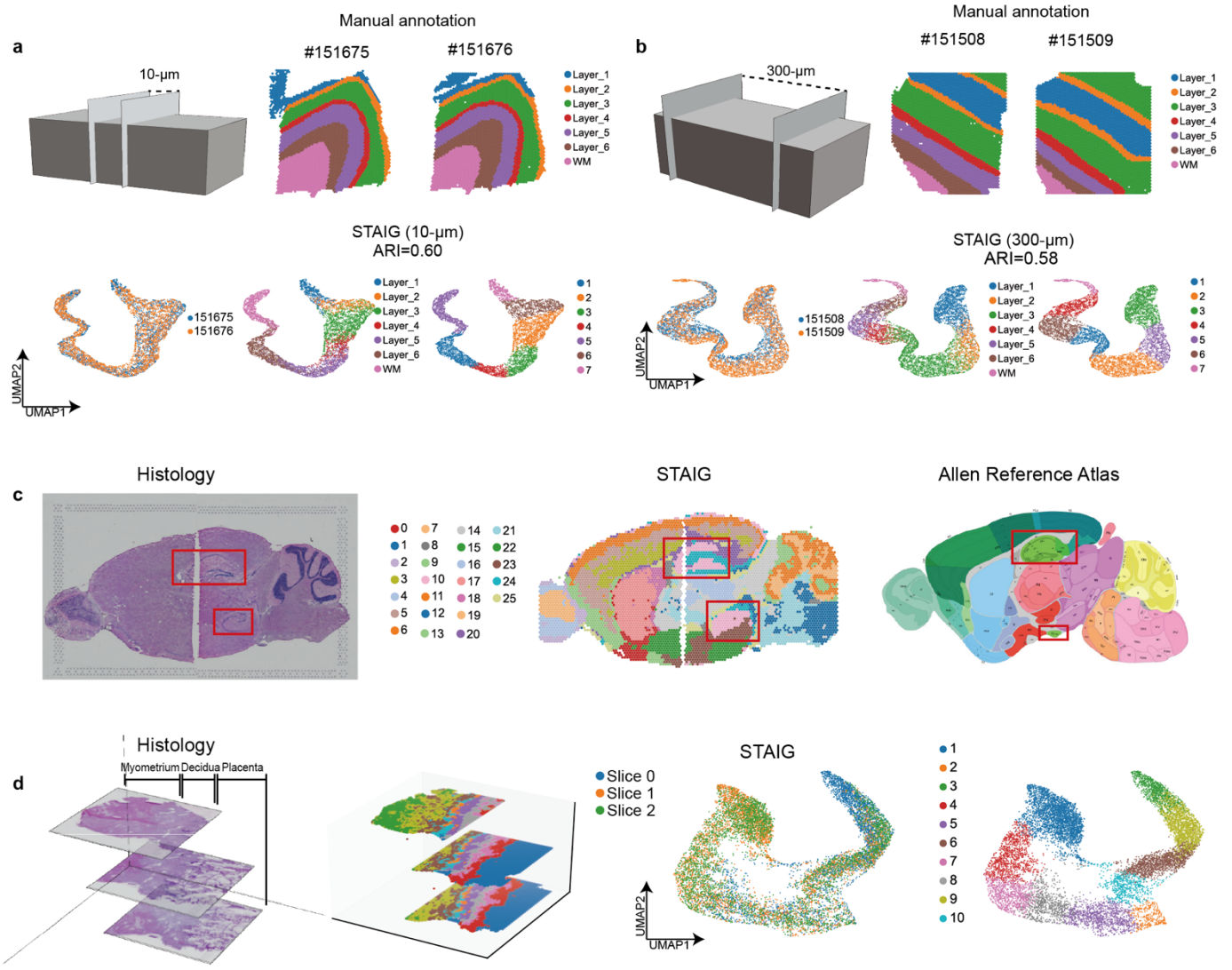

Fig. 5 Integration Capabilities of STAIG.

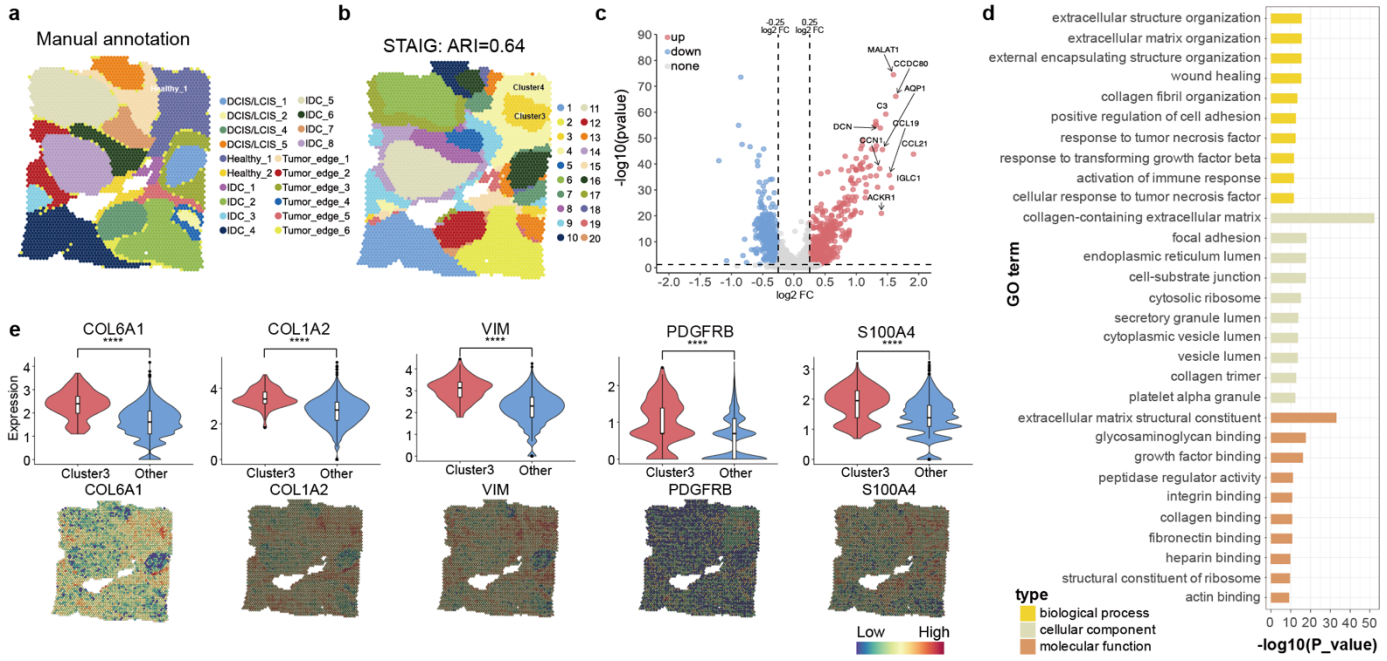

Fig. 6 Advanced spatial analysis by STAIG reveals Cancer-associated fibroblasts (CAF)-rich clusters in human Breast Cancer ST Data.

669

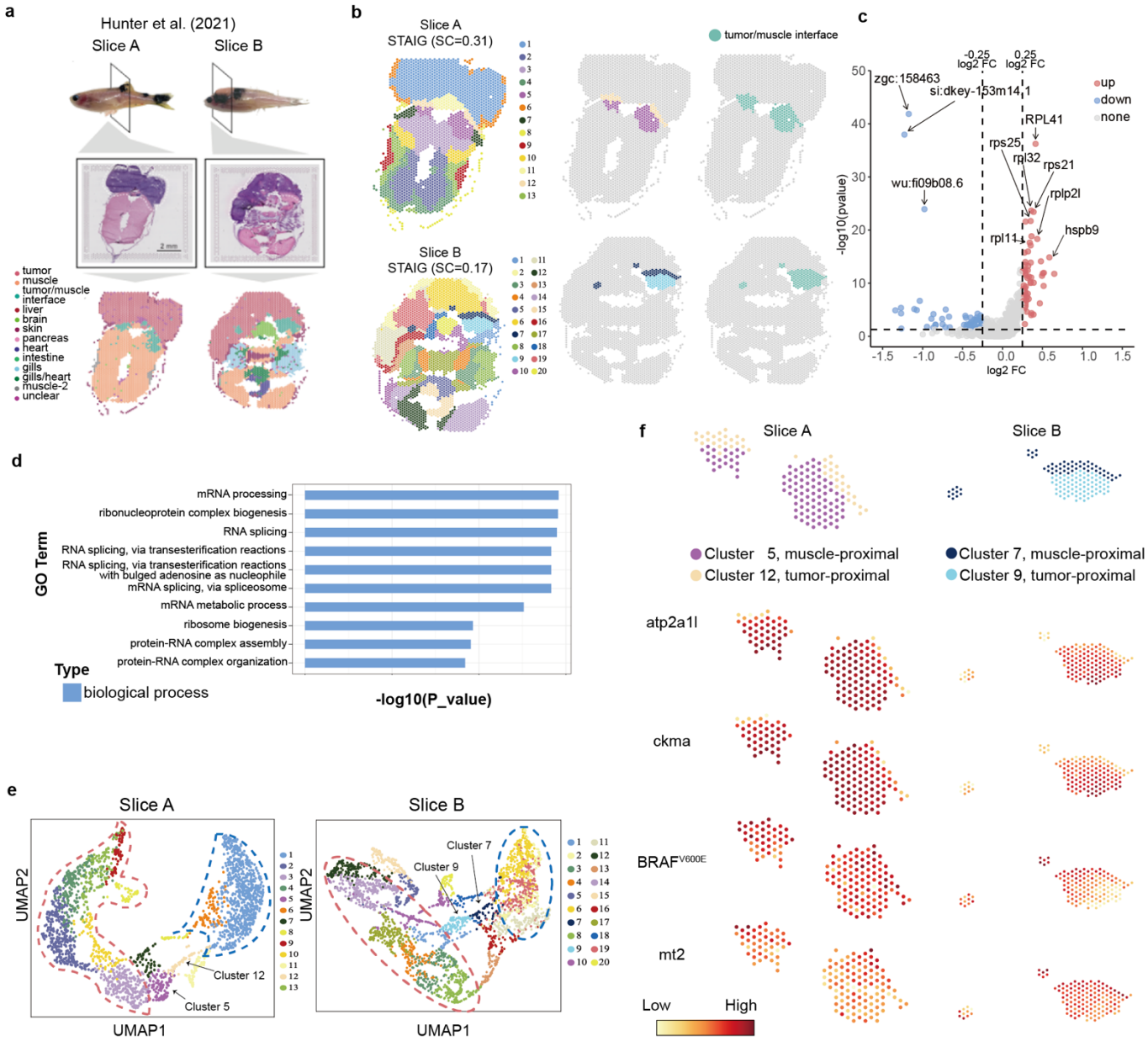

670

671 **Fig. 7 Enhanced resolution of tumor interface dynamics in zebrafish melanoma using STAIG analysis.**

672